Monthly Notices of the ROYAL ASTRONOMICAL SOCIETY

MNRAS **510,** 5579–5591 (2022) https://doi.org/10.1093/mnras/stac023
Advance Access publication 2022 January 10

Cosmic rays from massive star clusters: a close look at Westerlund 1

Sourav Bhadra [1,2]★ Siddhartha Gupta [3] Biman B. Nath [1] and Prateek Sharma [2]

[1]*Raman Research Institute, Sadashiva Nagar, Bangalore 560080, India*
[2]*Joint Astronomy Programme, Department of Physics, Indian Institute of Science, Bangalore 560012, India*
[3]*Department of Astronomy and Astrophysics, University of Chicago, IL 60637, USA*

Accepted 2021 December 23. Received 2021 December 13; in original form 2021 October 21

ABSTRACT

We study the effect of cosmic ray (CR) acceleration in the massive compact star cluster Westerlund 1 in light of its recent detection in γ-rays. Recent observations reveal a $1/r$ radial distribution of the CR energy density. Here, we theoretically investigate whether or not this profile can help to distinguish between (1) continuous CR acceleration in the star cluster stellar wind-driven shocks and (2) discrete CR acceleration in multiple supernovae (SNe) shocks – which are often debated in the literature. Using idealized two-fluid simulations and exploring different acceleration sites and diffusion coefficients, we obtain the CR energy density profile and luminosity to find the best match for the γ-ray observations. We find that the inferred CR energy density profiles from observations of γ-ray luminosity and mass can be much different from the true radial profile. CR acceleration at either the cluster core region or the wind termination shock can explain the observations, if the diffusion coefficient is $\kappa_{\rm cr} \sim 10^{27}\,{\rm cm^2\,s^{-1}}$ and a fraction of $\approx 10-20$ per cent of the shock power/post-shock pressure is deposited into the CR component. We also study the possibility of discrete SNe explosions being responsible for CR acceleration and find that with an injection rate of 1 SN in every $\sim$0.03 Myr, one can explain the observed γ-ray profile. This multiple SN scenario is consistent with X-ray observations only if the thermal conductivity is close to the Spitzer value.

Key words: ISM: bubbles – cosmic rays – gamma-rays: diffuse background – gamma-rays: ISM.

1 INTRODUCTION

There is a recent surge of interest in the acceleration of cosmic rays (CRs) in massive star clusters, which are increasingly seen as a supplementary site of CR acceleration in our Galaxy besides isolated supernova (SN) remnants. The γ-ray observations by *Fermi-LAT, HESS,* and *HAWC* have provided the evidence of hadronic acceleration in a handful of massive star clusters. For instance, the Cygnus OB association, Westerlund 1 (hereafter referred to as WD1), Westerlund 2 in our Galaxy, and 30 Doradus in the Large Magellanic Cloud are some of the bright sources of γ-rays from GeV to several TeV energies and have been interpreted as powerful CR accelerators (Abdo et al. 2010; Ackermann et al. 2011; Abramowski et al. 2015; Abeysekara et al. 2021). Although star-forming regions have been previously discussed as possible sources of CRs (e.g. Knödlseder 2013; Bykov 2014), these γ-ray observations have strengthened this hypothesis and they allow us to make more detailed theoretical models, thereby to improve our understanding of CR acceleration in these environments.

The idea that massive star clusters are potential acceleration sites of CRs has long been discussed in the literature, beginning with energetic arguments (Cesarsky & Montmerle 1983). CR acceleration in these environments can also solve many problems associated with the isolated SN paradigm, including proton acceleration up to $\sim$ PeV energies (representing the knee of the Galatic CR spectrum) and the excess of ^{22}Ne/^{20}Ne in CRs compared to the standard ISM composition (Higdon & Lingenfelter 2003, for a review, see Gabici et al. 2019). Detailed theoretical investigations support these predictions (e.g. Gupta et al. 2020; Morlino et al. 2021). In this regard, Gupta et al. (2020) have demonstrated that the problem of the large observed ratio of Neon isotopes (^{22}Ne/^{20}Ne) can be solved by invoking CR acceleration in the stellar winds in star clusters. Concurrently, it has been suggested from various phenomenological considerations that most of the observed CR grammage in the Galaxy is accumulated in star clusters, and not while propagating through the interstellar medium (ISM) at large (see e.g. Blasi & Serpico 2009; Cowsik & Madziwa-Nussinov 2016; Eichler 2017; Biermann et al. 2018). Taking this cue, Nath & Eichler (2020) have shown that the resulting γ-rays from star clusters can explain a significant fraction of the observed diffuse Galactic background. These developments prod us to look deeper at the individual and detailed observations of star clusters.

Recently, using the γ-ray observations of Cygnus and WD1 and CO/HI observations, Aharonian, Yang & Wilhelmi (2019, hereafter AYW19) reported that the spatial distribution of CR energy density in these objects follows $1/r$ profile. They suggested a steady injection (over $\sim$few Myr) of CRs instead of instantaneous injection as normally expected in the case of an isolated SN. Although such profiles can be derived by solving steady-state CR transport equation (cf. Section 2), it is worth mentioning that the steady-state assumption is questionable when the shock-bubble structure continuously evolves. We subject these observations to scrutiny with two-fluid hydro simulation and check if other interpretations (of the actual CR energy density profile and the mode of CR injection) are ruled out and if the

★ E-mail: souravbhadra@iisc.ac.in; sbhadra07@gmail.com

observations can be used to infer the relevant physical parameters for CR acceleration. In this work, we have studied different CR injection methods in order to understand the observed γ-ray luminosity, mass, and CR energy density of the WD1 cluster. We selected WD1 for our study mainly because it is a compact cluster and can be modelled convincingly using 1D simulations. Although there are a few other clusters that have been detected in γ-rays (such as Cygnus; Bartoli, Bernardini & Bi 2014), those objects are distinctly non-spherical in morphology and have substructures, which make them difficult to compare with 1D simulations. We begin with analytical estimates of γ-ray luminosity in Section 2. The numerical simulation setup is described in Section 3. In Section 4, we present our results, followed by further discussions in Section 5; and we summarize in Section 6.

2 PRELIMINARIES

In a couple of massive star clusters (e.g. WD1 cluster; see AYW19), the CR energy density in different annuli, as estimated from γ-ray luminosity, has been found to follow a $1/r$ profile. These profiles are often interpreted in terms of a steady injection of CRs (with energy E) from the dense core of compact star cluster with an energy-dependent CR diffusion [diffusion coefficient $\kappa_{\rm cr}(E)$]. This can be shown directly by using the CR diffusion-transport equation

$$\frac{\partial N(E)}{\partial t} = \kappa_{\rm cr}(E)\nabla^2 N(E) + Q(E), \tag{1}$$

where $N(E)$ is the number density of CRs and $Q(E)$ is their energy injection rate density. The energy moment of this equation can be written as

$$\frac{\partial e_{\rm cr}}{\partial t} = \kappa_{\rm cr}\nabla^2 e_{\rm cr} + \frac{L}{V}, \tag{2}$$

where $e_{\rm cr}$ represents CR energy density, $\kappa_{\rm cr}$ is an appropriately averaged diffusion coefficient for CRs, and $\frac{L}{V}$ the CR luminosity density. Let us assume that CR particles are injected in a small central region of radius r_0, which is much smaller in extent than the size of the star cluster. The rest of the volume is assumed to be devoid of CR production sites for simplicity. Therefore, except in the very central region, we need to solve the equation

$$\frac{\partial e_{\rm cr}}{\partial t} = \kappa_{\rm cr}\nabla^2 e_{\rm cr}\,. \tag{3}$$

In steady state, it reduces to (in spherical symmetry)

$$\frac{\rm d}{{\rm d}r}\left(r^2\frac{\rm d}{{\rm d}r}e_{\rm cr}\right) = 0\,, \Rightarrow e_{\rm cr} \propto \int\frac{{\rm d}r}{r^2}\,, \tag{4}$$

which has the solution $e_{\rm cr} = \frac{A}{r} + B$, where $B \to 0$ since the CR energy density is zero at infinity, and where A is a constant that depends on the boundary condition at r_0. This is the $1/r$ solution which is taken to be an evidence for steady injection of CR energy in massive clusters (AYW19).

Clearly, the above estimate neglects some crucial aspects such as (1) advection of CRs, (2) role of CR acceleration sites other than the central region, (3) losses due to radiative cooling of the gas, (4) projection effects, and (5) dominating γ-ray emission regions (which can be different from acceleration site; cf. 4.2). These considerations are important for the case of massive star clusters. Therefore, time-dependent numerical simulations are essential. Our two-fluid approach allows us to consider the wind termination shock (WTS) as an acceleration site, as well as to study the effect of time-varying CR/mechanical luminosity of the star cluster, including discrete SNe.

2.1 γ-ray luminosity (L_γ)

2.1.1 Hadronic contribution

One of the major sources of γ-rays in WD1 is the hadronic interaction between CR protons and protons in the ambient gas (see below for an estimate of γ-ray flux in the leptonic case, from inverse Compton scattering of stellar photons by CR electrons). The mechanism of production of γ-rays is

$$p + p \to p + p + \pi^0\,, \quad \pi^0 \to \gamma + \gamma. \tag{5}$$

Therefore, observations of γ-ray photons hold clue to the spatial distribution of CR protons.

To estimate γ-ray luminosity due to hadronic interactions, we use the prescription of Dermer's model (Dermer 1986; Pfrommer & Enßlin 2004), which yields the luminosity between ($E_{\gamma 1}$ and $E_{\gamma 2}$) energies

$$\begin{aligned} L_\gamma^H &= \int_V {\rm d}V \int_{E_{\gamma 1}}^{E_{\gamma 2}} {\rm d}E_\gamma\, E_\gamma\, q_\gamma(n_N, e_{\rm cr}, E_\gamma) \\ &= \int_V {\rm d}V\, n_N(r)\, e_{\rm cr}(r) \left[\int_{E_{\gamma 1}}^{E_{\gamma 2}} {\rm d}E_\gamma\, E_\gamma\, \tilde{q_\gamma}\right]. \end{aligned} \tag{6}$$

Here, $q_\gamma = {\rm d}N/({\rm d}t\,{\rm d}V\,{\rm d}E_\gamma)$ is the number of γ-ray photons emitted per unit volume per unit time per unit energy, which is proportional to the number density of target nucleon (n_N) and the CR energy density ($e_{\rm cr}$). The integration is to be carried over the entire volume of the emission region. The isotropic source function $\tilde{q_\gamma}$, used in the second integral, is given as (see e.g. Pfrommer & Enßlin 2004; Gupta et al. 2018; Jana, Roy & Nath 2020)

$$\tilde{q_\gamma} = \frac{\sigma_{pp} c \left(\frac{E_{\pi^0}}{GeV}\right)^{-\alpha_\gamma} \left[\left(\frac{2E_\gamma}{E_{\pi^0}}\right)^{\delta_\gamma} + \left(\frac{2E_\gamma}{E_{\pi^0}}\right)^{-\delta_\gamma}\right]^{-\frac{\alpha_\gamma}{\delta_\gamma}}}{\xi^{\alpha_\gamma - 2}\left(\frac{3\alpha_\gamma}{4}\right)\left(\frac{E_p}{(2\alpha_p - 2)\rm GeV}\right)\left(\frac{E_p}{\rm GeV}\right)^{1-\alpha_p}\beta\left(\frac{\alpha_p - 2}{2}, \frac{3-\alpha_p}{2}\right)}. \tag{7}$$

Here, $\xi = 2$ is the multiplicity factor, which denotes two leading pion jets leaving the interaction site, E_p and E_{π^0} are the rest mass energy of proton and pions (π^0), respectively. The spectral indices of the incident CR protons and emitted γ-ray photons are denoted by α_p and α_γ, respectively, $\delta_\gamma = 0.14\alpha_\gamma^{-1.6} + 0.44$ is the spectral shape parameter and $\sigma_{pp} = 32(0.96 + e^{4.4-2.4\alpha_\gamma})$ mbarn (for details, see equations 8 and 19–21 in Pfrommer & Enßlin 2004). We use $\alpha_\gamma = \alpha_p = 2.3$ following the spectral fit of Ackermann et al. (2015). The integration over the γ-ray photon energy in equation (6) for $E_{\gamma 1} = 1$ TeV and $E_{\gamma 2} = 100$ TeV (the contribution at higher energies is very small) gives $1.05 \times 10^{-17}\,{\rm cm^3\,s^{-1}}$. Thus, the γ -ray luminosity above 1 TeV can be written as

$$L_\gamma^H \sim 10^{-17}\left(\frac{\Delta V}{\rm cm^3}\right)\left(\frac{n_N}{\rm cm^{-3}}\right)\left(\frac{e_{\rm cr}}{\rm erg\,cm^{-3}}\right)\,{\rm erg\,s^{-1}}\,. \tag{8}$$

We use this equation to calculate the γ-ray luminosity from the relevant region of the cluster. On inverting equation (8), we get the CR energy density above 10 TeV,

$$\begin{aligned} e_{\rm cr}(>10{\rm TeV}) \approx 1.5 \times 10^{-2} &\left(\frac{L_\gamma^H}{10^{34}\,{\rm erg\,s^{-1}}}\right) \\ &\times \left(\frac{10^6\,{\rm M_\odot}}{M}\right){\rm eV\,cm^{-3}}, \end{aligned} \tag{9}$$

where M is the mass and L_γ is the γ-ray luminosity above 1 TeV energy.

2.1.2 Leptonic contribution

It is also possible to have a leptonic contribution to the total γ-ray luminosity, from inverse Compton scattering of stellar radiation photons by CR electrons, especially close to the star cluster where stellar photon density is significant. We estimate the leptonic emission as follows.

The energy density of CR electrons is assumed to be 0.01 of the total CR energy density (i.e. $e_{\rm cr,\,e} \approx 0.01 e_{\rm cr}$). This value has some uncertainty. From observations in the Solar system, at CR energy ~ 10 GeV, where solar modulation effects are low, the ratio of CR electron to proton energy is known to be 1 per cent (Longair 2011; section 15.1 of Schlickeiser 2002). Assuming the energy distribution of CR electrons to be $n(\Gamma) = \kappa_1 \Gamma^{-p}$ (in terms of the Lorentz factor Γ), where $p = 2.3$ (same as that of protons), the normalization constant κ_1 is given by

$$\kappa_1 \approx \frac{e_{\rm cr,e}}{m_e c^2}(p-2)\left[\frac{1}{\Gamma_L^{p-2}} - \frac{1}{\Gamma_U^{p-2}}\right]^{-1}. \tag{10}$$

Here, the upper cutoff to the Lorentz factor can be taken as $\Gamma_U \rightarrow \infty$ and the lower cutoff (Γ_L), as unity. Then, the total IC luminosity (which provides an upper limit to γ-ray luminosity) is given by Rybicki & Lightman (1979, equation 7.21)

$$L_\gamma^{IC} = \int_V {\rm d}V \left[\frac{4}{3}\sigma_T\, c\, e_{\rm ph}\, \kappa_1 \frac{\Gamma_{\rm max}^{3-p} - \Gamma_{\rm min}^{3-p}}{3-p}\right], \tag{11}$$

where, $e_{\rm ph}$ is the photon energy density, which at a distance r from the central core region of star cluster is given by

$$e_{\rm ph} = \frac{L_{\rm rad}}{4\pi r^2 c}. \tag{12}$$

Hence, one can obtain an upper limit to the leptonic contribution by using equations (10), (11), and (12).

Using these equations, one gets a sharply declining profile of L_γ with distance, because of the rapid decline of $e_{\rm ph}$ with radius. This is in contrast with the observed increasing profile of L_γ with projected distance. The observed profile therefore works against the leptonic interpretation of the origin of γ-rays.

Since IC scattering boosts the seed photon energy by a factor of Γ^2 (Γ being the electron Lorentz factor), a seed (stellar) photon of $\sim$1 eV will require $\Gamma = 10^6$ for it to be scattered into 1 TeV energy. If we take the photons in the waveband 0.01–100 eV (FIR to FUV), then the total radiation luminosity of the cluster is given by $L_{\rm rad} \sim 500 L_w$ (Leitherer et al. 1999), where L_w denotes the mechanical luminosity. In the innermost region considered here, within 9 pc, the photon energy density amounts to $\approx$1125 eV/cc. Therefore, electrons that do not cool within 4.5 Myr have $\Gamma \leq 120$, which require a seed photon energy of $\geq$70 MeV in order to up-scatter to 1 TeV. Note that this incident photon energy is much greater than our assumed seed photon energy (0.01–100 eV). Therefore, no photons in this region can be upscattered to above 1 TeV. If we put $\Gamma = 120$ as $\Gamma_{\rm max}$ and $\Gamma_{\rm min} = 1$ in equation (11), we get

$$L_\gamma^{IC} \sim 10^{-18}\left(\frac{L_w}{10^{39}{\rm erg\,s^{-1}}}\right)\left[\int {\rm d}V \left(\frac{r}{10{\rm pc}}\right)^{-2} e_{\rm cr}(r)\right] {\rm erg\,s^{-1}}, \tag{13}$$

where dV and $e_{\rm cr}$ are in cgs unit. A comparison with equation (8) shows that even *total* IC losses (only a negligible fraction of this is emitted above 1 TeV) are smaller than the hadronic luminosity above 1 TeV.

2.2 CR energy density ($e_{\rm cr}$)

Although our simulation can track the CR energy density $(e)_{\rm cr}$, observations can only determine it through projection, and that too indirectly using L_γ and the total projected mass in different projected annuli. In order to compare our calculations with observed parameters, we note that AYW19 have estimated the CR energy density $e_{\rm cr,\,inf}$ above 10 TeV using the following expression (their equation 7, which is almost identical to our equation 9)

$$e_{\rm cr,inf}(>10{\rm TeV}) = 1.8\times10^{-2}\left(\frac{\eta}{1.5}\right)\left(\frac{L_\gamma}{10^{34}\,{\rm erg\,s^{-1}}}\right) \times \left(\frac{10^6\,{\rm M_\odot}}{M}\right){\rm eV\,cm^{-3}}, \tag{14}$$

where M is the mass and L_γ is the γ-ray luminosity above 1 TeV energy. We use the subscript 'inf' to emphasize that this is the *inferred* value of CR energy density, in order to distinguish from the real value, which we get from simulation. η accounts for nuclei heavier than hydrogen in both CRs and ISM. Clearly, the value of η depends on the chemical composition of the ambient gas and CRs. The composition parameter η varies between 1.5 to 2 (Kafexhiu et al. 2014; Dermer 1986), and here we have used $\eta = 1.5$. Note that, we mainly consider those CRs which have energy more than 10 TeV in our calculations. Also note that the equations (9) and (14) are in good agreement.

2.3 Distance to WD1: recent updates and estimation of age

There has been an uncertainty regarding the distance to the WD1 cluster. AYW19 have used a distance of 4 kpc. However, the recent Gaia Early Data Release 3 (hereafter 'EDR3'; Aghakhanloo et al. 2021) has provided a more accurate determination of the distance of WD1, of 2.8 kpc, which is smaller than previously thought. All the distances we use in our simulation, as well as calculations, are based on the Gaia EDR3 (Aghakhanloo et al. 2021). The observed value of projected γ-ray luminosity, as well as projected mass, also have been modified accordingly. In other words, the physical sizes of the bins have been decreased by a factor of 4/2.8 = 1.42.

As far as the age is concerned, Aghakhanloo et al. (2021) stated that the turnoff mass will be reduced from 40 to 22 $M_\odot$, which would imply an increase in the age. However, Negueruela et al. (2010) found the turn-off mass to be $\sim$25 $M_\odot$, and the age, 4–5 Myr. Also, one can estimate the age from the relative number of Wolf–Rayet to Red Supergiants irrespective of the distance, and this yields an age of 4.5–5 Myr. Moreover, the age of WD1 cluster cannot be more than $\sim$5 Myr, since Wolf–Rayet stars cannot last longer than this (although Beasor et al. 2021 has claimed a much larger age of 7.2 Myr). Here, we use an age of 4.5 Myr, and we show our results at this epoch. The physical and simulation parameters for WD1 are in Table 1.

3 NUMERICAL SET UP

We use the publicly available magneto-hydrodynamics code, PLUTO (Mignone et al. 2007), our version of which supports CRs as a fluid detailed in Gupta, Sharma & Mignone (2021). PLUTO is a finite-volume Godunov code based on Riemann solvers, designed to integrate a system of conservation laws of fluid dynamics that adopts a structured mesh. In this work, the code solves the following set of equations

$$\frac{\partial\rho}{\partial t} + \nabla\cdot(\rho\boldsymbol{v}) = S_\rho, \tag{15a}$$

$$\frac{\partial(\rho\boldsymbol{v})}{\partial t} + \nabla\cdot(\rho\boldsymbol{v}\otimes\boldsymbol{v}) + \nabla(p_{\rm th} + p_{\rm cr}) = \rho\boldsymbol{g}, \tag{15b}$$

Table 1. Various physical and simulation parameters of WD1 used in this work.

Westerlund1			
Observations		Simulation parameters	
Extension (pc)	60	ϵ_{cr}/w_{cr} *range covered*	0.1−0.3
Age of cluster (Myr)	4−6	κ_{cr} *range covered*	$(5-100)\times10^{26}$ cm^2 s^{-1}
Kinetic Luminosity (erg s^{-1})	10^{39}	*Simulation box size*	250 pc
Distance (kpc)	2.8	*No. of grids*	5000
Mass-loss rate ($M_\odot$ yr^{-1})	7.5×10^{-4}	*Cooling*	Tabulated

$$\frac{\partial(e_{th}+e_k)}{\partial t}+\nabla[(e_{th}+e_k)\boldsymbol{v}]+\nabla[\boldsymbol{v}(p_{th}+p_{cr})] = p_{cr}\nabla\cdot\boldsymbol{v}-\nabla\cdot\boldsymbol{F}_{tc}+q_{eff}+S_{th}+\rho\boldsymbol{v}\cdot\boldsymbol{g}, \quad (15c)$$

$$\frac{\partial e_{cr}}{\partial t}+\nabla\cdot[e_{cr}\boldsymbol{v}] = -p_{cr}\nabla\cdot\boldsymbol{v}-\nabla\cdot\boldsymbol{F}_{crdiff}+S_{cr}, \quad (15d)$$

where ρ is the mass density, $\boldsymbol{v}$ is the fluid velocity, p_{th} and p_{cr} are thermal pressure and CR pressure, respectively. e_k is the kinetic energy density, $e_{th}=p_{th}/(\gamma_{th}-1)$ and $e_{cr}=p_{cr}/(\gamma_{cr}-1)$ are the thermal energy density and CR energy density, respectively. S_ρ, S_{th}, and S_{cr} are the mass and energy source terms per unit time per unit volume. $\boldsymbol{F}_{tc}$, $\boldsymbol{F}_{crdiff}$ represents thermal conduction flux and CR diffusion flux, respectively, g denotes the gravity and q_{eff} accounts for the radiative energy loss of the thermal gas. We have used HLL Riemann solver, piecewise linear reconstruction, and RK2 time-stepping. In our simulation, we use a CFL number of 0.4 and 1D spherical geometry.

3.1 Ambient medium

In the Section 2.1, we show that a major fraction of γ-rays can be produced due to hadronic interactions, and therefore, modelling the gas density of the cloud is crucial. However, the gas density in these environments is largely uncertain. Current observations provide us with the total mass up to a given radius and the projected density profile when the bubble has already evolved. With this limited information, we have explored various density distributions and finally selected a density profile (as briefly discussed below), which not only shows a good match with the total gas mass of WD1 (AYW19), but also gives a size of the bubble at ∼4.5 Myr comparable to observations.

We use a combination of self-gravitating isothermal clouds with solar metallicity following Section 4.1 in Gupta et al. (2018). This gives the total mass density at the central region of the cloud $\sim625\,m_H$ cm^{-3}, which drops radially as $\sim220(5\mathrm{pc}/r)\,m_H$ cm^{-3}; see e.g. their fig. 1, giving the mass $\sim10^6\,M_\odot$ for a cloud of radius $\approx$ 100 pc. These numbers are consistent with WD1. Note that, as soon as the wind/SNe becomes active, this initial density profile only remains valid outside the bubble. The interior structure evolves depending on the mechanical energy and mass injections from the star cluster, as we discuss in the following sections.

3.2 Wind driving region

The main driving engines in star clusters are stellar wind and SN explosions. While the stellar wind from individual stars can vary with time, the total wind power and mass can be assumed to be constant over time (Leitherer et al. 1999), which are mainly injected by massive stars located in the central regions of compact clusters such as WD1. Mass and energy are deposited in a spherical region of radius $r_{inj}=1$ pc around the centre (the volume of the injection region is $V_{src}=4/3\,\pi r_{inj}^3$) and the spatial resolution of the runs is $\Delta r=0.05$ pc. We set this resolution to minimize un-physical cooling losses (see Section 4 in Sharma et al. 2014). The injection region is chosen in such a way that the radiative energy loss rate is less than the energy injection rate (Sharma et al. 2014). In our simulations, we set the mass-loss rate $\dot{M}=7.5\times10^{-4}\,M_\odot$ yr^{-1} (Table 1) and kinetic luminosity $L_w=10^{39}$ erg s^{-1}. The mass-loss rate $\dot{M}$ in chosen so that the wind velocity $v\sim[2L_w/\dot{M}]^{1/2}$ for WD1 is nearly 2000 km s^{-1} (Chevalier & Clegg 1985). An injection parameter ϵ_{cr} (see equation 24) is used to specify the fraction of total injected energy given to CRs. The source term S_{cr} in equation (15d) can be expressed in terms of the kinetic luminosity of the source region

$$S_{cr}=\frac{\epsilon_{cr}L_w}{V_{src}}. \quad (16)$$

Similarly, S_ρ (in equation 15a) and S_{th} (in equation 15c) can be expressed as

$$S_\rho=\frac{\dot{M}}{V_{src}} \quad ; \quad S_{th}=\frac{(1-\epsilon_{cr})L_w}{V_{src}}. \quad (17)$$

3.3 CR injection

We consider three different methods of CR injection in this paper. In the first case, CRs are injected in the wind driving region, i.e. within r_{inj}. In the second case, CRs are injected into the shocked zones. The last case is a combination of both. These injection regions can be seen as possible CR acceleration sites in this object, where the central injection represents unresolved regions, e.g. colliding winds, which can also accelerate CRs (Eichler & Usov 1993; Bykov 2014). We use the following three conditions to identify the shocked zones (Pfrommer et al. 2017; Gupta et al. 2021)

$$\nabla\cdot\boldsymbol{v}<0, \quad (18)$$

$$\nabla p\cdot\frac{\Delta r}{p}>\delta_{threshold}, \quad (19)$$

$$\nabla T\cdot\nabla\rho>0. \quad (20)$$

Here, $\vec{v}$, p, ρ, and T are the velocity, pressure, density, and temperature of the fluid, respectively. The first condition selects compressed zones, the second condition sets the pressure jump at the shock, and the third condition avoids the contact discontinuity (CD). In the third injection method, we use the combined injection of CRs in the wind driving region as well as in the shocked region.

For all these different injection methods, the injection of CRs does not add any additional energy in the computational domain. The injection parameter (ϵ_{cr} or w_{cr}, see Section 4.2) just distributes a fraction of the total mechanical energy in the CRs either in the wind driving region or in the shocked regions.

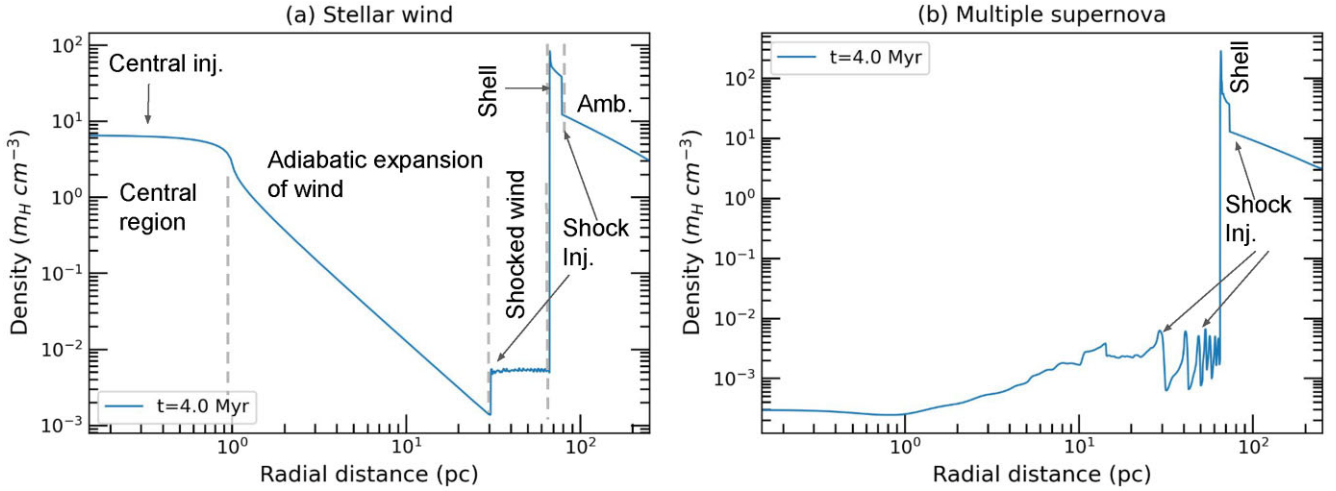

Figure 1. (a) Density profile of a wind-driven bubble at a time $t = 4.0$ Myr. The horizontal axis represents the distance from the centre in pc and the y-axis denotes the density in terms of m_H cm^{-3}, (b) density profile for multiple SN injection with SN frequency of 1 SN in each 3×10^4 yr. If we increase the SN frequency (i.e. one SN in each 1000 yr),then the density profile roughly takes the shape of continuous shell wind-like structure (shown in blue colour in the first panel of the lower row in Fig. 3). The label Central inj. in the figure denotes that CRs are injected at the central region and Shock inj. implies CRs are injected at shocks.

3.4 Microphysics

3.4.1 CR diffusion

Our simulations include the effects of CR diffusion. For numerical stability, diffusion typically has a much smaller time-step than the CFL time-step. To make our runs faster, we choose super time-stepping method (Alexiades, Amiez & Gremaud 1996) for the diffusion module, which sub-cycles CR diffusion for each hydro time-step. The CR diffusion flux term can be expressed in terms of CR energy density

$$\boldsymbol{F}_{\rm crdiff} = -\kappa_{\rm cr}\vec{\nabla}e_{\rm cr}\,, \tag{21}$$

where $\kappa_{\rm cr}$ is the diffusion coefficient and $e_{\rm cr}$ is the CR energy density. Generally, $\kappa_{\rm cr}$ is a function of CR energy, but here we consider a constant value of $\kappa_{\rm cr}$, which can be thought of as its appropriately energy weighted value across the energy distribution function of CRs (equation 7 in Drury & Voelk 1981).

We use a smaller value for the diffusion coefficient ($\kappa_{\rm cr}$) than generally used for the Galactic scales. We set $\kappa_{\rm cr}$ in the range of (5–100) $\times$ 10^{26} cm^2 s^{-1}. This is justified because CRs escaping the acceleration sites are expected to drive turbulence locally, making them diffuse more slowly compared to the ISM at large (Abeysekara et al. 2021).

3.4.2 Cooling

Radiative cooling that causes thermal energy loss of the gas is non-negligible in dense clouds. To include this, we use a tabulated cooling function corresponding to collisional equilibrium and solar metallicity (Sutherland & Dopita 1993; Ferland et al. 1998). A floor value in temperature is set to 10^4 K so that cooling is turned off when temperature $T < 10^4$ K, which arises from photoionization of the regions in the vicinity of the cluster (Gupta et al. 2016), on a spatial scale much larger than considered here. The ionized region around WD1 is larger than the outer radius of the cluster, thereby justifying the floor temperature value of 10^4 K. If S_* is the number of ionizing photons emitted per unit time by the star cluster, β_2 is the recombination coefficient of hydrogen (Case B approximation), and n_0 is the ambient density. The radius of the Strömgren sphere be R_S which is given by

$$R_S = \left(\frac{3}{4\pi}\frac{S_*}{n_0^2\beta_2}\right)^{1/3}. \tag{22}$$

If we use $n_0 = 50\,{\rm cm}^{-3}$, $S_* = 2.26 \times 10^{52}\,{\rm s}^{-1}$ (since the ionizing photon luminosity is $\approx 500 L_w$), $T = 10^4$ K, and $\beta_2 = 2 \times 10^{-13}\,{\rm cm}^3\,{\rm s}^{-1}$, one has the radius of Strömgren sphere as $\sim$50 pc. Instead of a uniform medium, if we take a $1/r$ -type radial ambient medium then the Strömgren radius will be much larger (the forward shock position is only slightly larger). The net heating is given by

$$q_{\rm eff} = -n_i n_e \Lambda_N + {\rm Heating}\,. \tag{23}$$

The heating of gas due to Coulomb interactions with CRs is negligible because the heating time-scale is larger than Gyr. We do not include heating due to CR streaming in our simulations, although we discuss its implications in Section 5.4.

4 RESULTS

We present our results in this section and then discuss the implications in Section 5.

4.1 Structure of star cluster driven bubble

Star clusters host massive stars as well as SN explosions, which produce a low-density bubble around them (Weaver et al. 1977; Gupta et al. 2018). Although the overall size of these bubbles (a few tens of pc) depends mainly on the total mechanical luminosity deposited by the cluster and the ambient density, the interior structure can qualitatively differ depending on whether the energy deposition is dominated by winds or SN explosions (Sharma et al. 2014). We discuss these differences below.

Fig. 1(a) shows the density profile of a stellar wind driven bubble (Weaver et al. 1977) at 4.0 Myr. There are four distinct regions in the plot: (1) the innermost portion contains the source of energy and mass deposition, (2) the free-wind region where the wind originating from the source expands adiabatically, (3) the shocked-wind region

containing slightly more dense gas, (4) the outermost shell containing the swept-up ambient gas. The shocked ISM and shocked wind regions are separated by a CD.

Fig. 1(b) shows the corresponding density profile for multiple SN injections, where one SN occurs every 3×10^4 yr. For this small rate, we do not observe any wind-like structure in the density profile, but if we increase the SN frequency, then the density profile does look similar to the case for continuous stellar wind (Blue curve in the first panel of the lower row in Fig. 3), with four distinct regions as mentioned earlier (Sharma et al. 2014).

The size of the bubble, or, to be precise, the distance to the CD is ≈80 pc, for an ambient density of $50 m_H\,\mathrm{cm}^{-3}$. This implies an extended γ-ray emission region of a similar size. Note that 80 pc at a distance of 2.8 kpc subtends an angle of $\approx 98'$. Indeed, the *HESS* excess map (AYW19, fig. 4 in their supplementary material) shows the γ-ray bright region to have a total extension of ≈3°, consistent with the above estimate for the angular radius. However, we note that roughly half of the last annulus (the fifth) drawn in the same figure by AYW19 is not γ-ray bright. This makes the γ-ray luminosity of the last projected bin comparable to the fourth bin and not brighter, which it would have been, if the γ-ray bright region had filled the last annulus. At the same time, the morphology of the γ-ray bright region shows that it is not spherically symmetric. Thus, although there is a rough agreement of the size of the bubble (and, consequently, the γ-ray bright region) from our spherically symmetric simulation with the size of the γ-ray bright region, a bin-by-bin matching of the simulated result with observations may not be possible.

Indeed, from the structure of the stellar wind bubble (Fig 1), it is clear that the swept-up shell is much denser than the interior of the bubble. This would result in an enhanced γ-ray luminosity for the outer radial bin, which would, in turn, dominate the projected luminosity in all projected bins.

4.2 Different acceleration sites and corresponding observables

As mentioned earlier, we consider three different CR acceleration sites in our simulations: (1) CR energy injection in the central wind region (using $\epsilon_{\rm cr}$), (2) injection at the shocks (using $w_{\rm cr}$), and (3) combined injection at shocks as well as the central wind region (using both $\epsilon_{\rm cr}$ and $w_{\rm cr}$). We compare our results with the observations of AYW19, albeit for a distance of 2.8 kpc to WD1 as described in Section 2.3. We discuss the effect of varying the distance in Appendix A1.

4.2.1 Central injection

In this scenario, CRs are injected into the source region, after which they diffuse outwards. The kinetic luminosity of the stellar wind is distributed in CRs and thermal energy. We define the injection parameter $\epsilon_{\rm cr}$ as

$$\epsilon_{\rm cr} = \frac{E_{\rm cr}}{E_{\rm IN}}\,, \tag{24}$$

where $E_{\rm cr}$ is the energy deposited in CRs and $E_{\rm IN}$ is the total deposited energy into the injection region.

We calculated the projected γ-ray luminosity and mass by dividing the cluster region into five bins from 0−45 pc with a width of 9 pc for each bin to compare with the observations of AYW19. While calculating the projected γ-ray luminosity, we have considered only the hadronic contribution since the leptonic contribution is relatively lower in magnitude than the hadronic contribution.

The fourth column plots the *inferred* CR energy density profile[1] in the same manner that observers would have done, based on the projected luminosity and mass. This has been done in order to bring out the essential difference between the actual radial profile (plotted in the first column of Fig. 2) and the inferred projected profile of CR energy density, the demonstration of which is the crux of this paper.

Note that AYW19 calculated the errors in CR density without considering the uncertainty in the mass estimates (which was mentioned as ∼50 per cent). This has resulted in the underestimation of the errors in the inferred CR energy density. We have therefore considered the error in the mass estimates while calculating the final errors in CR energy density. It is found that the revised error bars accommodate a flatter CR energy density profile than expected from a projection of $1/r$ profile. We note that the error mainly arises from the uncertainty in the conversion factor between CO and H_2, and its value at length scales as small as ∼50 pc remains unknown.

After exploring the parameter space, we have found that for a $1/r$ type radial profile of ambient density with the core density of $625\,m_H\,\mathrm{cm}^{-3}$ as discussed in Section 3.1, the best-fitting parameters are $\kappa_{\rm cr} = 3 \times 10^{27}\,\mathrm{cm}^2\,\mathrm{s}^{-1}$ and $\epsilon_{\rm cr} = 0.1$ (upper row of Fig. 2).

The projected γ-ray luminosity (above 1 TeV) and mass profiles are shown in the second and third column, respectively in Fig. 2, for all three different CR injection sites. It is clear from this figure that with proper choice of parameters, one can explain the observed values with a $1/r$ -type ambient profile. Note that we calculated the projected profiles for the whole simulation box i.e. 300 pc. If we use a simulation box of 400 pc instead of 300 pc, the γ -ray luminosity changes by (5 − 7) per cent.

4.2.2 Injection at the shock

Next, we consider the case of CR injection at strong shocks. We mainly consider injection at the WTS as the Mach number of WTS is much larger than the forward shock (FS); i.e. WTS is stronger than FS. The efficacy of CR injection at the shocks is described by a commonly used parameter (Chevalier 1983; Bell et al. 2014)

$$w_{\rm cr} = \frac{p_{\rm cr}}{p_{\rm th} + p_{\rm cr}}\,, \tag{25}$$

where $p_{\rm cr}$ and $p_{\rm th}$ are the CR and thermal pressures, respectively (similar as mentioned in Section 3). The downstream CR pressure fraction is therefore $p_{\rm cr} = w_{\rm cr}\, p_{\rm tot}$ (here, $p_{\rm tot} = p_{\rm cr} + p_{\rm th}$).

After a detailed study of the parameter space, we found that the best-fitting parameters that can explain the observational data are $\kappa_{\rm cr} = 10^{27}\ \mathrm{cm}^2\,\mathrm{s}^{-1}$ and $w_{\rm cr} = 0.2$ (consistent with ion acceleration efficiency found in kinetic simulations; see e.g. Caprioli & Spitkovsky 2014). The middle row of Fig. 2 shows the projected mass and γ-ray luminosity for these parameters. If we compare with the central injection case (uppermost panel), it is clear that shock injection requires a lower value of $\kappa_{\rm cr}$ than central injection in order to explain the observed γ-ray luminosity.

4.2.3 Combined injection

We also considered a CR injection scenario where CRs are accelerated in the source region as well as at the shocks. In this case of combined injection, $\epsilon_{\rm cr}$ parametrizes the fraction of kinetic energy that goes into CRs and $w_{\rm cr}$ decides how much of the downstream

[1]This is the inferred CR energy density at a given projected distance (details in Section 2.2).

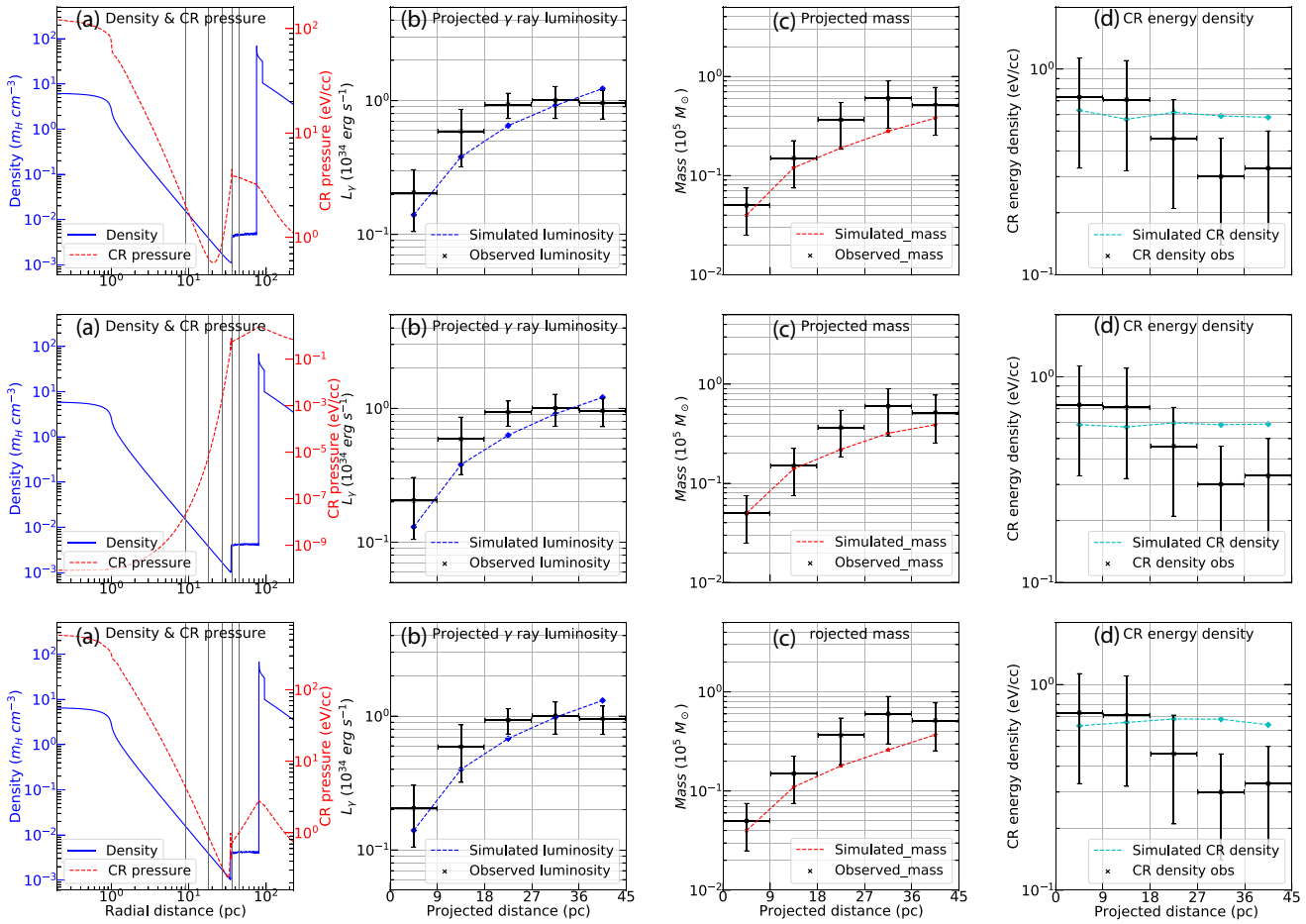

Figure 2. Results of simulations with the $1/r$ ambient density profile and different injection scenarios are displayed. We plot the radial density and CR pressure profiles (a), the projected γ-ray luminosity above 1 TeV (b), projected mass (c), and inferred CR energy density above 10 TeV ($e_{\rm cr,\,inf}$) (d) for different injection sites of CRs. Black data points with error bars represent observational data and the blue, red, and cyan dashed lines show the simulation results for luminosity, mass, and CR density, respectively. The vertical lines in panel (a) represent different projection bins. All profiles are shown at 4.5 Myr. The uppermost row shows the case of central injection with $\kappa_{\rm cr} = 3 \times 10^{27}$ cm^2 s^{-1} $\epsilon_{\rm cr} = 0.1$. The middle row shows the case of shock injection with $\kappa_{\rm cr} = 10^{27}$ cm^2 s^{-1}, $w_{\rm cr} = 0.2$. The bottom row shows the case of combined injection of CRs, and for $\kappa_{\rm cr} = 10^{27}$ cm^2 s^{-1}, $\epsilon_{\rm cr} = w_{\rm cr} = 0.2$. The parameters are chosen to match the γ-ray luminosity and mass profiles in different scenarios.

Table 2. Best-fitting parameters for different CR injection method.

Injection sites	Diffusion co-eff ($\kappa_{\rm cr}$) cm^2 s^{-1}	Injection parameter ($\epsilon_{\rm cr}$ or $w_{\rm cr}$)
Central injection	3×10^{27}	0.1
Shock injection	10^{27}	0.2
Combined injection	10^{27}	0.2

pressure is converted into CR pressure (same as in Sections 4.2.1 and 4.2.2 respectively). The best-matched profiles with observations are shown in the bottom row of the Fig. 2. The corresponding value of parameters are $\kappa_{\rm cr} = 10^{27}$ cm^2 s^{-1}, and $w_{\rm cr} = \epsilon_{\rm cr} = 0.2$. In Table 2, we have mentioned the best-fitting values of parameters which can explain the observed γ-ray and mass profile.

4.3 Multiple discrete supernova injection

Multiple discrete SNe can also produce stellar wind-like structures if the frequency of SNe is large (e.g. see fig. 12 in Yadav et al. 2017) and we have considered this alternative as well. For this, the mechanical luminosity L_w will correspond to a kinetic energy of 10^{51} erg per SNe, multiplied by the frequency of SNe. AYW19 suggested an SN rate of one SN every 1000 yr to support the quasi-continuous injection of CRs in the source region and to explain the observed CR density profile. However, this large rate of SNe is not realistic, because this implies $\approx 3 \times 10^4$ SNe in 30 Myr (corresponding to the main sequence lifetime of a 8-$M_\odot$ star), which would correspond to a total stellar mass of $\geq 3 \times 10^6$ $M_\odot$. Therefore, we performed simulations with a more realistic SN injection frequency of 0.03 Myr^{-1}, corresponding to the observed cluster stellar mass of 10^5 $M_\odot$.

Fig. 3 shows the corresponding projected luminosity, mass and inferred CR energy density profile for multiple SNe. For the above mentioned realistic SNe rate, the density profile, shown in the first panel of upper row of Fig. 3, does not show a stellar wind like structure (first panel of the lower row of Fig. 3), which is achieved only for a high rate of SN (*e.g.* 1 SN in every 1000 yr) (lower row of fig 3). Yet, one can get a close enough match with the projected luminosity and mass profiles. The best-fitting parameters for SNe rate of 0.03 Myr^{-1} are $\kappa_{\rm cr} = 5 \times 10^{27}$ cm^2 s^{-1}, $\epsilon_{\rm cr} = 0.1$, for an

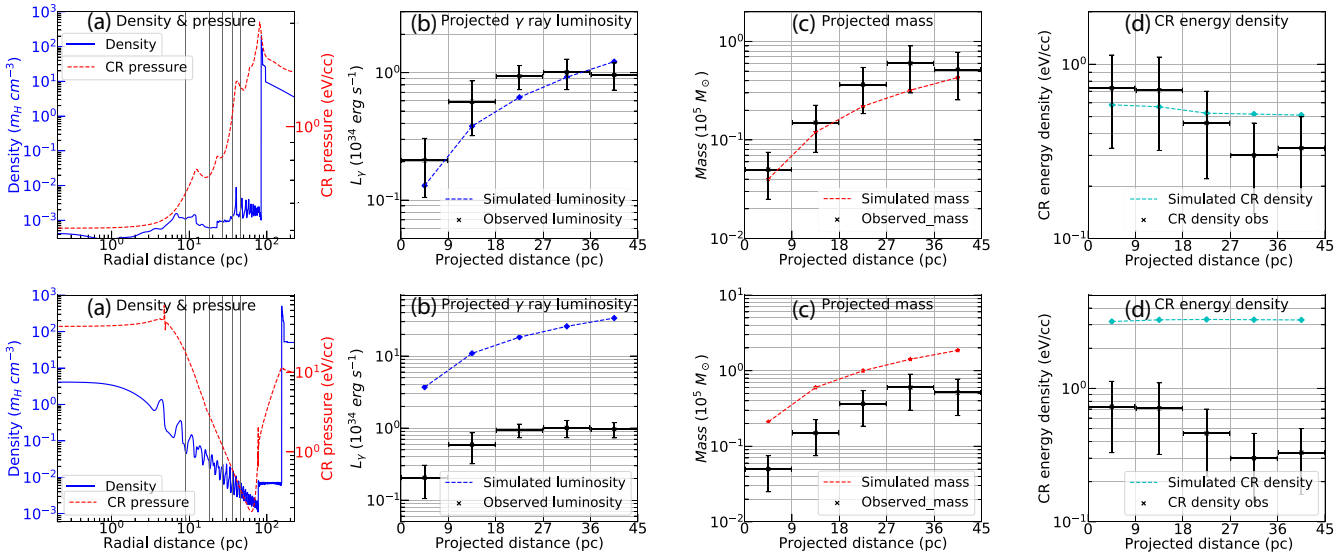

Figure 3. Profiles of the density and CR pressure, projected γ-ray luminosity (>1 TeV), mass, CR energy density above 10 TeV for the multiple discrete SN injection scenario. CRs are injected at the shocks detected by our shock detection method. The value of $\kappa_{cr} = 5 \times 10^{27}$ cm^2 s^{-1} and $\epsilon_{cr} = 0.1$. Upper row: one SN in every 0.03 Myr, lower row: one SN in every 1000 yr. Only the small SN rate, consistent with the cluster mass, can satisfy the observational constraints. For the lower panel, we have used a uniform density of 50 m_H cm^{-3} otherwise, for a 1/r type ambient, the FS position will be at a very large distance which does not match with the observation.

1/r -type ambient density. When the SNe rate is increased, the corresponding luminosity, mass, and inferred CR energy density profile much exceed the observed values. We have included this high rate of SN just to look at the prediction of AYW19 assumption. Also, for this high SNe rate, we have used a uniform ambient medium of 50 m_H cm^{-3}. Instead, if we use a 1/r type ambient medium, the outer shock position will be at a large distance (beyond ∼220 pc) which does not match the observation.

5 DISCUSSION

Our simulated γ-ray luminosity and mass profiles match the observations [panels (b) and (c) of Fig. 2], for the parameter values mentioned in each case of CR injection. We also note that the inferred CR energy density offers a good match with the observed profiles, in light of the revised error bars that include the uncertainty in mass estimation [panel (d) in each row of Fig. 2]. It should also be noted that our simulations are based on some simple assumptions e.g. spherical symmetry and constant diffusion coefficient. Three-dimensional simulations can produce more realistic morphology, but those require additional free parameters such as mass distribution of cloud and location of stars. It is therefore reasonable to say that the present simulations offer a good match with the observations, in light of all the uncertainties mentioned earlier.

There are other circumstantial reasons why a flatter CR energy density profile should be considered. Recently Abeysekara et al. (2021) have shown (in their fig. 2b) that for Cygnus cluster, the CR energy density above 10 TeV does not strictly follow a 1/r profile, and their observation does not rule out $e_{cr,\,inf}$ being uniform, which would make it consistent with our simulation results [panel (d) in each row of Fig. 2]. At the same time, the CR energy density profile for 100 GeV does follow 1/r profile (AYW19). Abeysekara et al. (2021) interpreted this absence of a 1/r profile for TeV CRs on the basis of larger diffusion rate for higher energy CRs.

The comparison of L_γ and $e_{cr,\,inf}$ from our simulation and observations indicate that the last projected bin is observed to be less

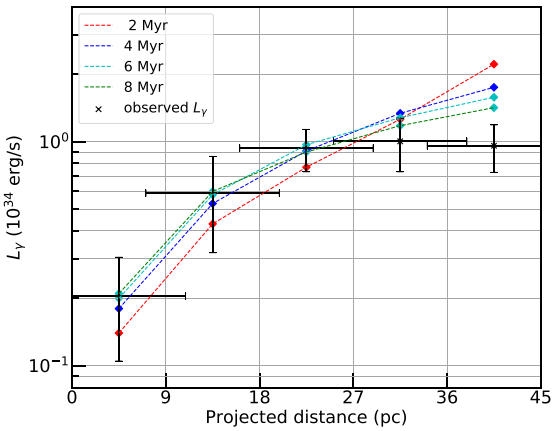

Figure 4. Time evolution of γ-ray luminosity for combined injection with $\kappa_{cr} = 10^{27}$ cm^2 s^{-1}, $w_{cr} = \epsilon_{cr} = 0.2$. Black points are from observation.

luminous than expected from simulation. There can be a variety of reasons for this discrepancy. One possibility is that the outer shell is fragmented and is porous, as in the case of 30 Doradus, for example (which allows the X-ray from the shocked wind region to be seen through the holes in the outer shell). Such a fragmented outer shell may make the γ-ray luminosity in the outer-most bin discrepant from the simulated values.

5.1 Time dependence of gamma-ray profiles

Fig. 4 shows the time dependency of the γ-ray luminosity profile for combined injection of CRs. As time increases, the bubble structure expands. The luminosity in the inner bins increases with time, but the outer bin shows an opposite trend. This is because, as time progresses, the outer shock covers a more extended region, thereby increasing the effective volume of the emitting region, and increasing the luminosity in the inner bins, because of the projection effect. At

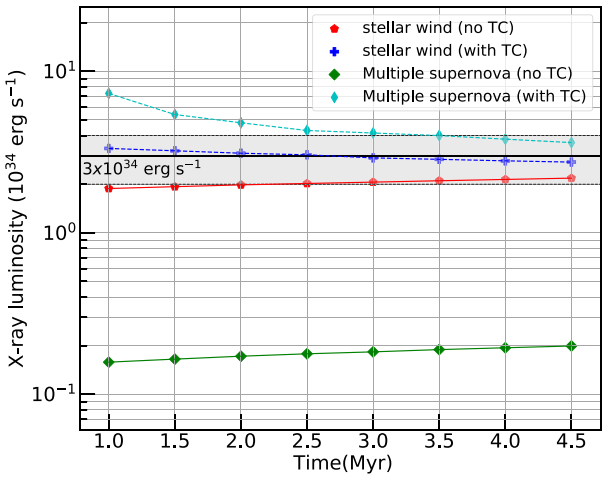

Figure 5. Time evolution of X-ray luminosity (2−8 keV) for stellar wind case (red and blue curves) and multiple SN case (green and cyan lines). The black solid line shows 3×10^{34} erg s^{-1} which is the obtained value from observation. The shaded region shows the range of the observed luminosity. Solid and dashed curves correspond to without TC runs and with TC runs, respectively.

the same time, the WTS and the shocked wind region gradually move out of the intermediate and outer bins, thereby decreasing the contributions in luminosity in those bins. The difference in the luminosity from 2 to 4 Myr is found to be roughly ∼25 per cent and within the observational margin of error.

5.2 Effect of thermal conduction

We have also studied the effect of thermal conduction on the simulated γ-ray profiles. We use thermal conduction to have the spitzer value ($\kappa_{\rm th} = 6 \times 10^{-7} T^{5/2}$ in CGS, Spitzer 1962) and also assumes the saturated thermal conduction (section 4.3 of Gupta et al. 2016). For the two-fluid model, thermal conduction does not significantly change the simulated γ-ray profile and the change in the γ-ray luminosity in each bin is $\leq (5-7)$ per cent.

5.3 Thermal X-rays

We have calculated the resulting X-ray luminosity of the (hot and dense) shocked wind region. We consider the X-ray emission due to thermal bremsstrahlung, which can be calculated using (equation 5.14b of Rybicki & Lightman 1979)

$$L_x = \int_V {\rm d}V \int_\nu {\rm d}\nu \left[6.8 \times 10^{-38}\, Z^2\, n_e\, n_i\, T^{-1/2}\, e^{-h\nu/kT}\, \tilde{g_{\rm ff}}\right]. \quad (26)$$

We take $n_e \sim n_p = P_{\rm th}/k_B T$ ($P_{\rm th}$ is the thermal pressure), $Z \sim 1$, and $\tilde{g_{\rm ff}} = 1.2$. The X-ray luminosity in 2−8 keV for both stellar wind and multiple SN cases is shown in Fig. 5. For stellar wind scenario, the X-ray luminosity matches the observed value (Muno et al. 2006) of $(3 \pm 1) \times 10^{34}$ erg s^{-1} (shown by the shaded region) with or without thermal conduction. However, the corresponding X-ray luminosity for the multiple SN injection scenario is more than one order lower in magnitude than the observed value if we do not include thermal conduction. This is due to the very low density of the gas (see Fig. 1b) inside the bubble, owing to the low SNe rate. (Higher SNe rate would recover the density structure, but overproduce γ-rays, as shown in the bottom panel of Fig. 3). However, with thermal conduction, the simulated values (cyan curve in the plot) are close to the shaded region for this injection scenario. For this case, we have set an upper limit of conduction coefficient, which corresponds to 10^7 K temperature (otherwise, the stability time-scale due to thermal conduction is too short). Therefore, both the stellar wind and multiple SN injection models can explain the observed γ-ray as well as X-ray luminosity.

5.4 Heating due to CRs and CR energy loss

CR energy loss, due to Coulomb and hadronic interactions, can indeed be important, as estimated below. Using the expressions for Coulomb and hadronic loss in Guo & Oh (2008), the total CR energy loss rate is

$$\Gamma_c = 7.6 \times 10^{-16} \left(\frac{n}{\rm cm^{-3}}\right) \left(\frac{e_{\rm cr}}{\rm erg\,cm^{-3}}\right) {\rm erg\,s^{-1}cm^{-3}}. \quad (27)$$

The heating time for the gas is

$$t_H \approx \frac{1.5 nkT}{(1.65 \times 10^{-16}\, n\, e_{\rm cr})}\ {\rm sec}, \quad (28)$$

considering only the Coulomb interaction. Using $e_{\rm cr} \sim 0.45$ eV cm^{-3}, $T = 10^4$ K (corresponds to shell temperature), the heating time scale is $t_H \sim 10^9$ yr. This heating time is much larger than the dynamical time-scale of 4.5 Myr, so the effect of this heating is negligible for the thermal gas. However, the energy loss time-scale for CRs is

$$t_{\rm cr,loss} \approx 0.4\,{\rm Myr} \left(\frac{n}{50\,{\rm m_H\,cm^{-3}}}\right)^{-1}. \quad (29)$$

We can also estimate the energy loss due to CR streaming heating, for which the heating rate is given by

$$\Gamma_{\rm streaming} = -v_A \cdot \nabla p_{\rm cr}\ {\rm erg\,cm^{-3}\,s^{-1}}. \quad (30)$$

Here, $p_{\rm cr}$ is the CR pressure and v_A is the Alfven velocity. If we assume equipartition of magnetic and thermal energy density, then $v_A \approx 1.3 \times 10^8$ cm s^{-1}. If we consider the region between 20–50 pc in the density plot [panel (a) of the topmost row of Fig. 2, we find that the change of CR pressure ($\Delta p_{\rm cr}$) is $\approx 1.8 \times 10^{-11}$ dyne cm^{-2} over a distance (Δr) of 30 pc. This gives us, $\Gamma_{\rm streaming} \approx 2.6 \times 10^{-23}$ erg cm^{-3} s^{-1}. The energy loss time-scale for CR is long, but the heating time-scale for the gas is ∼0.2 Myr, (for $n \approx 0.01$ cm^{-3}). Although this may be important, we have not included streaming heating in our simulations because it will involve making assumptions about the uncertain small-scale magnetic fields.

The above discussion, especially regarding the energy loss time-scale for CR (equation 29), shows that CR energy density in the shocked wind and outer shell can significantly decrease over the considered dynamical time-scale. This process would reduce the CR energy density in these regions and consequently decrease L_γ. Therefore, L_γ would be lower than presented here, especially in the outer bins, and make the inferred CR energy density decline with the projected distance. This may result in a better match with the observations.

Our analysis shows that the diffusion coefficient ($\kappa_{\rm cr}$) lies in the range of $(5-30) \times 10^{26}$ cm^2 s^{-1}. Note that CR diffusion is ineffective for a much lower diffusion coefficient, whereas CRs rapidly diffuse out of the bubble without affecting it if $\kappa_{\rm cr}$ is increased (see also Gupta et al. 2018). A comparison of the simulation results with observation implies that the γ-ray luminosity matches well if CR energy fraction $10-20$ per cent of the total input energy, consistent with theoretical expectations from diffuse shock acceleration mechanisms.

Also, note that the γ-ray luminosity is a function of both gas density (n_N) and CR energy density ($e_{\rm cr}$), whereas the mass is only a

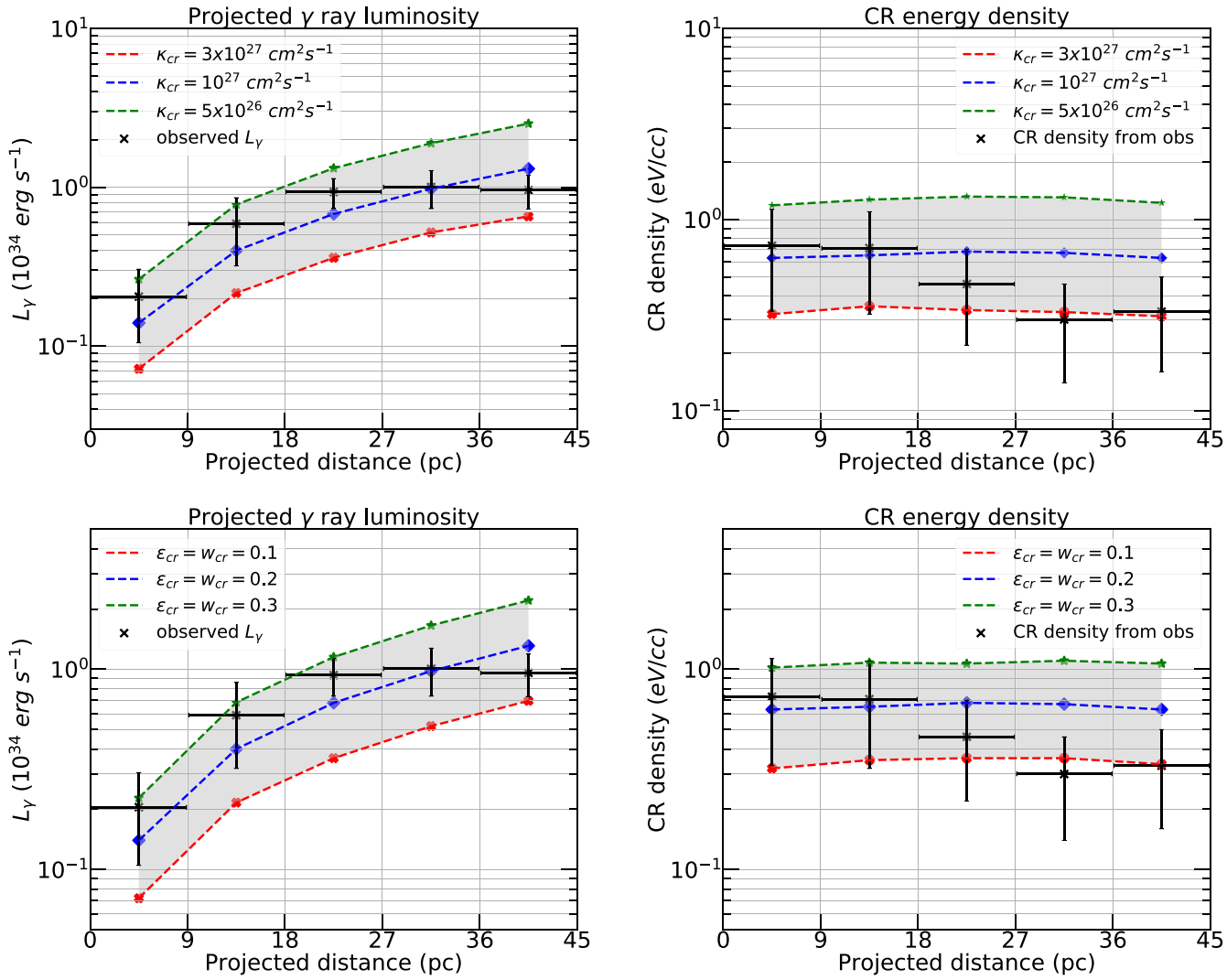

Figure 6. The projected γ-ray luminosity and inferred CR energy density profiles as a function of the projected radius for different injection parameters and diffusion parameters for the case of combined CR injection scenario. In all panels, black points with error bars indicate the observational values. The upper left- and right-hand panels show the variation of the γ-ray luminosity and inferred CR energy density for different $\kappa_{\rm cr}$, respectively for a fixed $w_{\rm cr} = \epsilon_{\rm cr} = 0.2$. The lower left-hand panel shows the variation of the γ-ray profile with varying CR injection parameter and the lower right-hand panel shows the variation of the projected inferred CR energy density profile with varying injection parameter. For the lower two panels, the value of $\kappa_{\rm cr} = 10^{27}$ cm^2 s^{-1}.

function of gas density. As $e_{\rm cr}$ depends on $\kappa_{\rm cr}$, the γ-ray luminosity changes significantly with a change in the diffusion coefficient, as shown in the upper left-hand panel of Fig. 6. In contrast, the mass profile does not strongly depend on our choice of parameters. For example, although the size of a stellar wind bubble depends on $\epsilon_{\rm cr}$, the projected mass does not change noticeably like the γ-ray luminosity for different values of $\epsilon_{\rm cr}$.

5.5 Dependence on various parameters

We have studied the dependence of our results on different parameters, *viz.*, the diffusion coefficient and the injection parameters.

5.5.1 Diffusion coefficient (κ_{cr})

To understand the effect of diffusion coefficient on the γ-ray profile, we also ran the simulations for different values of the diffusion coefficient, keeping a constant $\epsilon_{\rm cr} = w_{\rm cr} = 0.2$. The upper left- and right-hand panel of Fig. 6, respectively, show the variation of γ-ray luminosity and CR density with distance for different values of $\kappa_{\rm cr}$. It is clear from the upper left-hand panel of the same figure, the γ-ray luminosity exceeds the observed values for a lower value of diffusion coefficient. This is because a slower diffusion of CRs implies a higher density of CRs in the vicinity of the cluster, which increases the γ-ray luminosity.

The upper left-hand panel of Fig. 6 shows the corresponding variation of the inferred CR energy density profile with $\kappa_{\rm cr}$. As expected, increasing the diffusion coefficient depletes the injection region of CRs, and the resulting drained CR energy density profile is naturally decreased. However, our exercise selects the range of $\kappa_{\rm cr} \approx (5\text{–}100) \times 10^{26}$ cm^2 s^{-1} as the appropriate one since the observed values are bracketed from both sides in this range, as seen from the the upper left- and upper right-hand panels of Fig. 6. We note that this range of $\kappa_{\rm cr}$ is consistent with previous estimates from observations of γ-rays in star clusters (Gabici et al. 2010; Giuliani et al. 2010; Li & Chen 2010; Ackermann et al. 2011).

5.5.2 *Injection parameter ($w_{\rm cr}$ and ϵ_{cr})*

We have also run the simulations for different values of the injection parameter ($w_{\rm cr}$ and $\kappa_{\rm cr}$) keeping a constant diffusion coefficient $\kappa_{\rm cr} = 10^{27}\,{\rm cm^2\,s^{-1}}$. The lower left- and right-hand panels of Fig. 6, respectively, show the variation of γ-ray luminosity and CR density with distance for different injection parameters. It is clear from the lower left-hand panel of the figure that an increasing value of $w_{\rm cr}$ or $\epsilon_{\rm cr}$ increases the γ-ray luminosity, because a larger injection parameter means a larger fraction of kinetic energy being deposited into CRs which consequently increases the γ-ray luminosity in the close vicinity of the cluster. The corresponding CR density profile is shown in the lower right-hand panel of the Fig. 6.

6 CONCLUSIONS

We have studied the implication of the recently inferred distribution of CR energy density in massive compact star clusters, taking the particular example of WD1. With 1D two-fluid hydro-dynamical simulation for stellar wind in star clusters, we have studied the projected γ-ray luminosity, mass, and CR energy density for the WD1 cluster and their dependence on diffusion coefficient, injection parameter, and ambient density. Our findings are as follows:

(i) The most important takeaway from our analysis is that the inferred $1/r$ profile of CR energy density need not reflect its true radial profile. Also, we have shown that even the observed data can accommodate a flatter CR energy density profile, in light of revised error estimates. We have shown that dividing the projected L_γ by the projected mass in different annuli can yield a CR energy density profile that is significantly different from the actual profile. We have also pointed out various uncertainties that would make a straightforward inference difficult, *e.g.* the lack of morphological symmetry, the uncertainty in the mass estimate.

(ii) While a $1/r$ profile for the CR energy density allows a simple explanation in terms of a steady-state CR luminosity at the centre of the cluster, which makes it appealing, we have studied the more plausible scenarios, that of a time-varying CR luminosity, or CR being injected outside the central region (in the WTS, for example), and showed how these scenarios are also consistent with observations. We can not rule out any of the CR acceleration sites on the basis of these observations because the observed luminosity and mass profile can be explained by all three CR injection methods, as well as the discrete SN scenario by appropriate choice of the diffusion coefficient and injection parameters.

(iii) The parameters for the best match with observations are not ad-hoc, but are supported by independent arguments. For example, a lower value of diffusion coefficient ($10^{27}\,{\rm cm^2\,s^{-1}}$) can explain the observation for shock injection case, while for central injection a higher value ($3 \times 10^{27}\,{\rm cm^2\,s^{-1}}$) is required. These values for the diffusion coefficient are consistent with previous findings. The same goes for the parameter describing the efficiency of CR energy injection, which is found to be in the range $\epsilon_{\rm cr}/w_{\rm cr} \sim 0.1$–$0.3$, consistent with previous works (Gupta et al. 2018).

(iv) The discrete multiple SN injection scenario can explain the γ-ray observation with the appropriate choice of parameters. On the other hand, the simulated X-ray luminosity (assuming it to be thermal) is close to the observed value only if we include thermal conduction.

ACKNOWLEDGEMENTS

We would like to thank Manami Roy, Ranita Jana, Alankar Dutta for the valuable discussion. BBN would like to thank Felix Aharonian, Ruizhi Yang, Binita Hona for useful discussion on the data. We thank our anonymous referee for helpful comments. SB acknowledges Prime Minister's Research Fellowship (PMRF), Government of India for the financial support. PS acknowledges a Swarnajayanti Fellowship (DST/SJF/PSA-03/2016-17) and a National Supercomputing Mission (NSM) grant from the Department of Science and Technology, India.

DATA AVAILABILITY

The data not explicitly presented in the paper will be available upon reasonable request from the first author.

REFERENCES

Abdo A. A. et al., 2010, A&A, 512, A7
Abeysekara A. U. et al., 2021, Nat. Astron., 5, 724
Abramowski A. et al., 2015, Science, 347, 406
Ackermann M. et al., 2011, Science, 334, 1103
Ackermann M. et al., 2015, ApJ, 799, 86
Aghakhanloo M. et al., 2021, RNAAS, 5, 14
Aharonian F., Yang R., Wilhelmi E. O., 2019, Nature, 3, 561
Alexiades V., Amiez G., Gremaud P.-A., 1996, Num. Meth. Eng., 12, 31
Bartoli B., Bernardini P., Bi X. J., 2014, ApJ, 790, 152
Beasor E. R., Davies B., Smith N., Gehrz R. D., Figer D. F., 2021, ApJ, 912, 16B
Bell A. R., Araudo A. T., Matthews J. H., Blundell K. M., 2014, MNRAS, 447, 2224
Biermann P. L., 2018, ASR, 62, 2773
Blasi P., Serpico P. D., 2009, PRL, 103, 081103
Bykov A. M., 2014, A&A Rev., 22, 77
Caprioli D., Spitkovsky A., 2014, ApJ, 783, 91
Cesarsky C. J., Montmerle T., 1983, SSRv, 36, 173
Chevalier R. A., 1983, ApJ, 272, 765
Chevalier R. A., Clegg A. W., 1985, Nature, 6032, 44
Cowsik R., Madziwa-Nussinov T., 2016, ApJ, 827, 119
Dermer C. D., 1986, A&A, 157, 223
Dermer C. D., 1986, ApJ, 307, 47
Drury L. O., Voelk J. H., 1981, ApJ, 248, 344
Eichler D., 2017, ApJ, 842, 50
Eichler D., Usov V., 1993, ApJ, 402, 271
Ferland G. J., Korista K. T., Verner D. A., Ferguson J. W., Kingdon J. B., Verner E. M., 1998, PASP, 110, 761
Gabici S., Evoli C., Gaggero D., Lipari P., et al., 2019, Int. J. Mod. Phys. D, 28, 1930022
Gabici S., Casanova S., Aharonian F. A., Rowell G., 2010, SF2A-2010: Proceedings of the Annual meeting of the French Society of Astronomy and Astrophysics. p. 313
Giuliani A. et al., 2010, A&A, 516, 11
Guo F., Oh S. P., 2008, MNRAS, 384, 251
Gupta S., Nath B. B., Sharma P., Shchekinov Y., 2016, MNRAS, 462, 4532
Gupta S., Nath B. B., Sharma P., 2018, MNRAS, 479, 5220
Gupta S., Nath B. B., Sharma P., Eichler D., 2020, MNRAS, 493, 3159
Gupta S., Sharma P., Mignone A., 2021, MNRAS, 502, 2733
Higdon J. C., Lingenfelter R. E., 2003, ApJ, 590, 822
Jana R., Roy M., Nath B. B., 2020, ApJ, 903, L9
Kafexhiu E., Aharonian F., Taylor A. M., Vila G. S., 2014, Phys. Rev. D, 90, 12
Knödlseder J., 2013, ASSP, 34, 169
Leitherer C. et al., 1999, ApJS, 123, 3
Li H., Chen Y., 2010, MNRAS, 409, 35
Longair M. S., 2011, High Energy Astrophysics. Cambridge University Press, Cambridge
Mignone A., Bodo G., Massaglia S., Matsakos T., Tesileanu O., Zanni C., Ferrari A., 2007, MNRAS, 170, 228
Morlino G., Blasi P., Peretti E., Cristofari P., 2021, MNRAS, 504, 6096

Muno M. P., Law C., Clark J. S., Dougherty S. M., de Grijs R., Portegies Zwart S., Yusef-Zadeh F., 2006, ApJ, 650, 203
Nath B. B., Eichler D., 2020, MNRAS, 499, L1
Negueruela I., González-Fernández C., Marco A., Clark J. S., Martínez-Núñez S., 2010, A&A, 513, A74
Pfrommer C., Enßlin T. A., 2004, A&A, 413, 17
Pfrommer C., Pakmor R., Schaal K., Simpson C. M., Springel V., 2017, MNRAS, 465, 4500
Rybicki G. B., Lightman A. P., 1979, Radiative Processes in Astrophysics, Wiley, New York
Schlickeiser R., 2002, Cosmic Ray Astrophysics, Springer, Berlin, p. 472
Sharma P., Roy A., Nath B. B., Shchekinov Y., 2014, MNRAS, 443, 3463
Spitzer L., 1962, Physics of Fully Ionized Gases, Interscience, New York
Sutherland R. S., Dopita M. A., 1993, ApJS, 88, 253
Weaver R., McCray R., Castor J., Shapiro P., Moore R., 1977, ApJ, 218, 377
Yadav N., Mukherjee D., Sharma P., Nath B. B., 2017, MNRAS, 465, 1720

APPENDIX A: EFFECT OF DISTANCE OF WD1

In this work, we have used a distance of 2.8 kpc for WD1, but it is important to know how the difference in distance affects the inferences, because previous works assumed it to be 4 kpc. For this reason, we have determined the projected γ-ray luminosity and mass for a distance of 4 kpc (which is 1.4 times larger than the new predicted distance of 2.8 kpc). As a consequence of this, the observed γ-ray luminosity, as well as the projected mass, will increase by a factor of $1.4^2 \approx 2$ for each bin. Also, the width of the bin will increase 1.4 times and each bin width will become 13 pc instead of 9 pc that we have used in our calculations in the main text. If we consider a bin of projected distance between w_1 and w_2, then the total projected luminosity in the bin is calculated by integrating over this region (i.e. from w_1 to w_2)

$$L_{w_1 \to w_2} = 2\pi \int_{w_1}^{w_2} \left[\int_{w_1}^{r_{box}} 2 j_\nu(r) \frac{r\,\mathrm{d}r}{\sqrt{r^2 - w^2}} \right] w\ \mathrm{d}w\,,$$

where j_ν is the emissivity, $r_{\rm box}$ is the maximum box size, and r is the radial distance. A change in the distance will modify the bin width and will affect the γ-ray luminosity through the above integral. Since the projected mass is calculated in a similar way, the mass estimate will also change in a similar way.

Fig. A1 shows the corresponding profiles for a distance of 4 kpc distance, for the case of combined CR injection. Upon comparison with the bottom panel of Fig. 2, we find that the modified projected L_γ and projected mass are still within the observational error bars. The CR energy density does not deviate much from the limit of error bar of the data points. To summarize, the effect of changing the distance is rather modest in light of the observational uncertainties and does not significantly affect the conclusions.

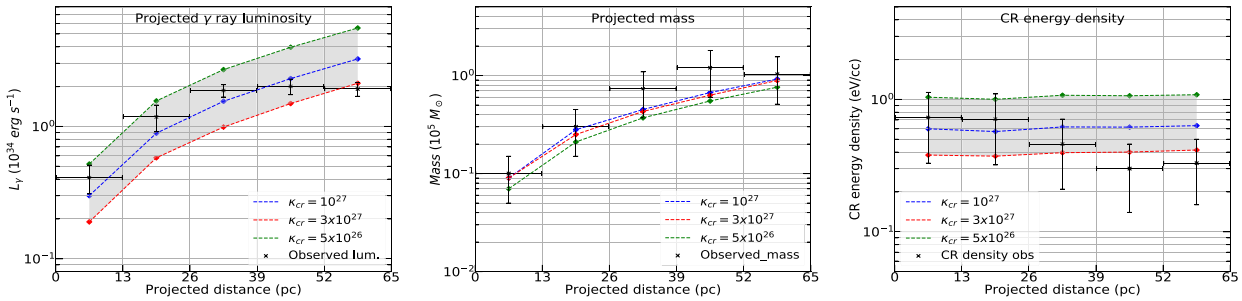

Figure A1. Same as in the bottom row of Fig. 2, except that a distance of WD1 is taken to be 4 kpc. The effect of varying $\kappa_{\rm cr}$ is also shown in the figure.

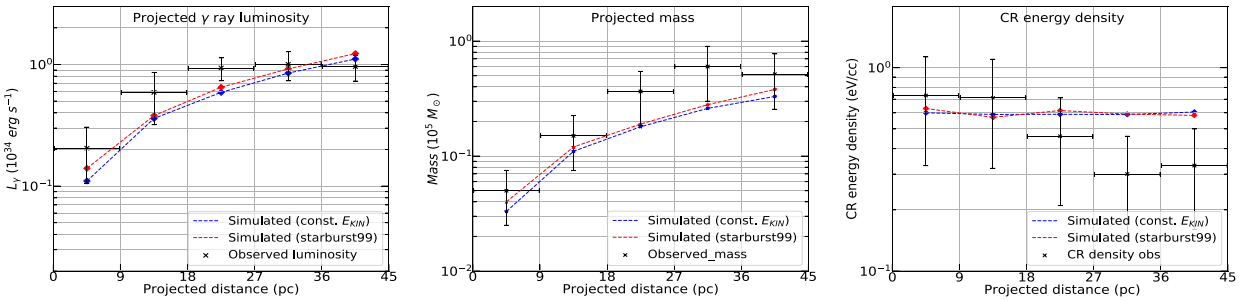

Figure B1. Variation of projected γ-ray luminosity above 1 TeV, mass and CR energy density above 10 TeV as a function of projected distance for central CR injection scenario. The red curve is for STARBURST99 model and the blue curve is for constant mechanical luminosity driven model. The match between the two is very close.

APPENDIX B: EFFECT OF TIME-VARYING MECHANICAL LUMINOSITY: STARBURST99

We have also investigated the effect of the time-dependent mechanical luminosity of the cluster, L_w, using STARBURST99[2] (Leitherer et al. 1999), which is a publicly available code for stellar evolution in clusters. We use the Padova AGB track with solar metallicity and instantaneous star formation for this calculation. In Fig. B1, we compare our result with the case of a constant mechanical luminosity-driven wind model. We find that these two models do not differ much in terms of projected luminosity, mass, or inferred CR energy density. Here, the parameters used are $\kappa_{\rm cr} = 3 \times 10^{27}$ cm^2 s^{-1}, $\epsilon_{\rm cr} = 0.1$ for central injection of CRs.

[2]https://www.stsci.edu/science/starburst99/docs/default.htm

This paper has been typeset from a TEX/LATEX file prepared by the author.